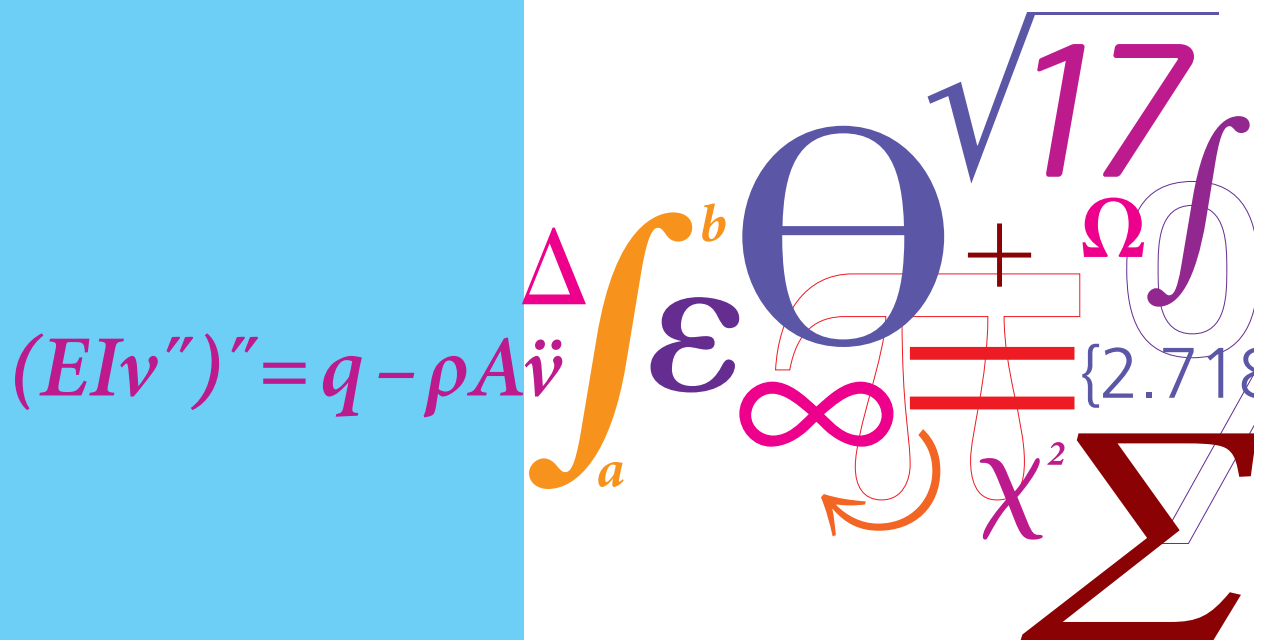


# Numerical Simulation of Turbulent Round Jet

BSc.Eng. Project



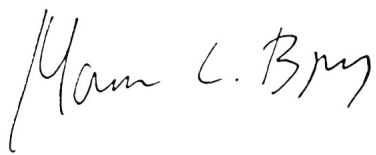
Morten Bjerg  
June 2018

## Preface

This is a 15 ECTS Bachelor thesis within the Department of Mechanical Engineering at the Technical University of Denmark. The project was carried out under the supervision of DTU Professor Jens Honore Walther and co-supervisor PhD student Azur Hodzic.

Thank you Jens and Azur for taking the time to patiently guide me through this project.

Morten Bjerg

A handwritten signature in black ink, reading "Morten L. Bjerg". The signature is written in a cursive style, with the first letter 'M' being large and stylized, and the last name 'Bjerg' written in a more fluid, connected script.

## Abstract

This Bachelor thesis investigates the turbulent round jet. The term jet vaguely defines a fluid discharging through an orifice into a larger body of fluid. Jets are widely used in industrial processes and can look very different depending on the particular application. However, in this study the turbulent round jet was investigated in its most generic form: a flat velocity profile issuing from a wall-mounted orifice into a quiescent space of the same fluid. Inspired by Boersma et al. [2], the jet was simulated at a low Reynolds number of 2400 by means of direct numerical simulation (DNS) and the simulations were carried out using the open source software OpenFOAM. Mean flow statistics such as the centreline decay constant, the half-radius spreading rate, and the self-similar axial profiles are in strong correspondence with the results of Boersma et al. [2]. However, it was found necessary to disturb the inflow with uncorrelated noise to achieve turbulence at the given Reynolds number even though Boersma et al. [2] report that they obtained a so-called natural transition to turbulence. Apart from the DNS, a large eddy simulation (LES) was carried out using a local dynamic one-equation eddy viscosity model. It was the intention to assess the potential of this model to accurately describe a jet flow at a higher Reynolds number, as it was the initial scope of the project to eventually simulate a jet at a Reynolds number of 20,000. The results of the LES simulations were promising though further work is required to determine if the LES is comparable to the DNS simulation. Relevant material from the project is available at GitHub: [https://github.com/mbjerg/Turbulent\\_Jet](https://github.com/mbjerg/Turbulent_Jet).

# Contents

<b>1</b>	<b>Introduction</b>	<b>1</b>
1.1	Motivation . . . . .	1
1.2	Report Structure . . . . .	1
1.3	General Theory of Turbulent Jets . . . . .	2
1.3.1	Centreline Velocity . . . . .	2
1.3.2	Near-, Intermediate-, and Far Field . . . . .	3
1.3.3	Spreading Rate . . . . .	4
1.3.4	The Kolmogorov Length Scale . . . . .	5
<b>2</b>	<b>Method</b>	<b>7</b>
2.1	Pre-processing . . . . .	7
2.1.1	Domain . . . . .	7
2.1.2	Gmsh . . . . .	8
2.1.3	Mesh Design . . . . .	8
2.2	Simulation Configuration . . . . .	11
2.2.1	OpenFOAM . . . . .	11
2.2.2	Governing Equations . . . . .	11
2.2.3	Numerical Method . . . . .	11
2.2.4	Boundary Conditions . . . . .	12
2.2.5	Initial Condition . . . . .	15
2.2.6	Temporal Resolution . . . . .	15
2.3	Post-processing . . . . .	16
<b>3</b>	<b>Results and Discussion</b>	<b>17</b>
3.1	DNS . . . . .	17
3.2	LES . . . . .	24
<b>4</b>	<b>Conclusion</b>	<b>27</b>
<b>5</b>	<b>Further Work</b>	<b>28</b>
	<b>References</b>	<b>29</b>
	<b>Appendix</b>	<b>29</b>
A	Axial Evolution of the Kolmogorov Length Scale . . . . .	30
B	Derivation of The Kolmogorov Length Scale Growth . . . . .	31
C	Contraction Profile Momentum Flux . . . . .	32

# Nomenclature

## Symbols

$A$	Slope of the half-radius spreading rate function
$B$	Intersection of the half-radius spreading rate function
$B_u$	Centreline decay constant
$Co$	Courant number
$D$	Orifice diameter
NIF	Near-Intermediate-Field
$p$	Pressure
$R$	Jet radius
$r$	Radial coordinate
$r_{1/2}$	Jet half-radius
$Re$	Reynolds number
$\mathbf{u}$	Three-component velocity vector
$U_c$	Local centreline velocity
$U_{jet}$	Jet inlet velocity
$U_{ref}$	Contraction profile constant
$z$	Axial coordinate
$z_0$	Virtual origin
$\epsilon$	Turbulence dissipation rate
$\delta_{1/2}$	Jet half-width
$\delta t$	Time step
$\delta z$	Axial cell dimension
$\eta$	Self-similarity coordinate
$\eta_k$	The Kolmogorov length scale
$\nu$	Kinematic viscosity
$\rho$	Density

## Abbreviations

PISO	Pressure-Implicit with Splitting of Operators
LES	Large eddy simulation
DNS	Direct numerical simulation

# 1 Introduction

## 1.1 Motivation

The turbulent round jet is of interest both within industry and academia. The turbulent jet is an integrated part of a wide range of industrial processes such as chemical mixing and combustion. Thus an increased understanding of the nature of turbulent jets contributes to technological improvements in numerous engineering disciplines. However, this project is not related to one particular practical application. From an academic perspective the turbulent jet serves as a canonical flow case to reveal the nature of free shear flows and for testing numerical solution methods. Despite the extensive research within the field turbulence it remains a poorly understood physical phenomenon.

The aim of this study is to examine the turbulent jet in its most generic form: a flat velocity profile shooting from an orifice into a quiescent space. Inspired by Boersma et al. (1998) [2], the spatial development of the jet is simulated using direct numerical simulation (DNS) at a modest Reynolds number of 2400. Hence Navier-Stokes equations in incompressible form are directly solved without the use of any turbulence modelling. Mean flow statistics are compared with the results obtained by Boersma et al. [2] as those results show excellent agreement with experimental results such as those obtained by Panchapakesan and Lumley (1993) [5]. Furthermore, a large eddy simulation (LES) using a local dynamic one-equation eddy viscosity model is also performed in an attempt to replicate the results of Boersma et al. [2] with less computational power than required for a DNS simulation. The initial scope of the project was to eventually compare a LES simulation at a Reynolds number of 20,000 with measurements obtained by supervisor PhD student Azur Hodzic. However, it proved to be challenging enough to simply replicate the results of Boersma et al. [2].

## 1.2 Report Structure

This report begins with a brief description of the turbulent round jet and the associated terminology. The General Theory section is then followed by the Method section which covers the setup of the simulations and the reasoning behind the choice of domain, mesh, boundary conditions, initial condition, and numerical method. The most important findings are then presented in the Results and Discussion section and compared with the results of Boersma et al. [2]. Relevant material from the project such as images, post-processing data, and mesh files are uploaded to a public repository on GitHub: [https://github.com/mbjerg/Turbulent\\_Jet](https://github.com/mbjerg/Turbulent_Jet).

### 1.3 General Theory of Turbulent Jets

This section covers some general theory on turbulent jets and is based on the Ball et al. [1] review of both experimental and computational studies of round turbulent jets as well as turbulence theory from Stephen B. Pope's [6] classic textbook on turbulent flows. In its simplest form, a jet is a Newtonian fluid exiting a nozzle producing an approximately flat velocity profile. The fluid is flowing into an ambient of the same fluid. The round jet is fully defined by the Reynolds number based on jet inlet velocity, inlet diameter, and the kinematic viscosity. Figure 1 shows the half-cross-sectional view of the turbulent round jet in its most generic form: a flat-topped velocity profile emerging from an orifice bounded by a wall. In most industrial applications the jet is shooting from a nozzle, however, the flow characteristics are to some degree dependent on the type of nozzle. Thus it is more generic to use a wall-mounted orifice to remove the unknown influence of a particular nozzle shape.

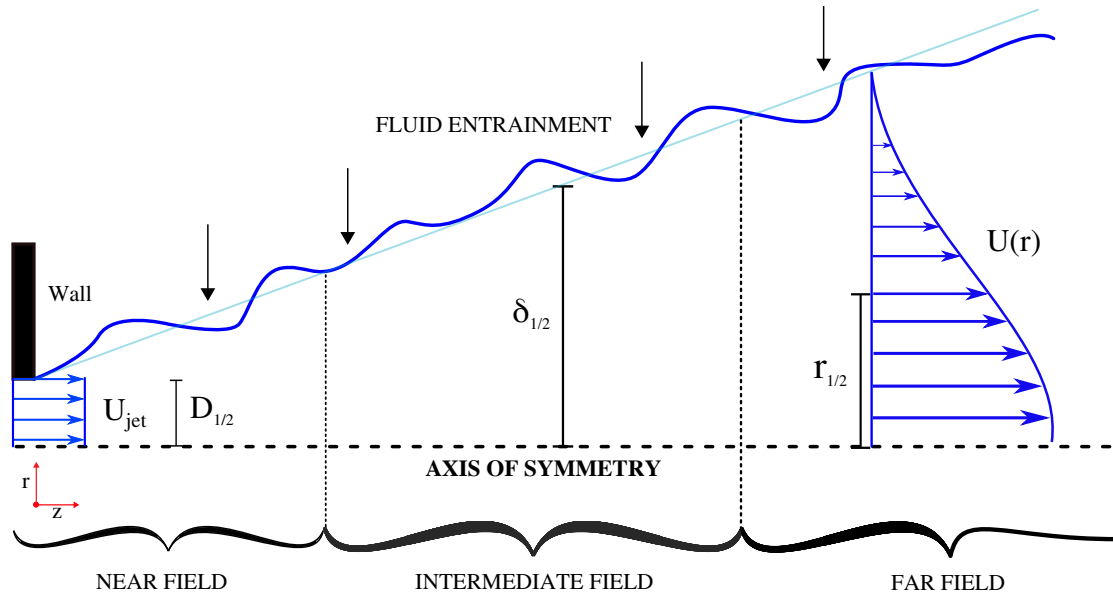


**Figure 1:** Half-cross-sectional view of a turbulent round jet originating from a wall-mounted orifice. The illustration shows the downstream growth of the jet as ambient fluid is entrained in the jet.  $U_{\text{jet}}$  is the bulk inlet velocity,  $D$  is the jet diameter,  $\delta_{1/2}$  is the half-width of the jet, and  $r_{1/2}$  is the so-called half-radius.

#### 1.3.1 Centreline Velocity

The centreline velocity normalized with the bulk jet velocity,  $U_{\text{jet}}$ , has a very characteristic shape when plotted as a function of the axial distance normalized by the jet diameter,  $D$  (Figure 2). Several jet diameters of axial distance from the jet origin, the jet remains almost intact and  $U_c/U_{\text{jet}} \approx 1$ . Then an instability in the interface between the jet and the quiescent ambient fluid leads to the jet breakup characterized by a sudden drop in centreline velocity. From this point and on, the centreline velocity starts to decay according to equation (1). Figure 2 illustrates the jet centreline velocity as well as the inverse of the centreline velocity as a function of axial distance.

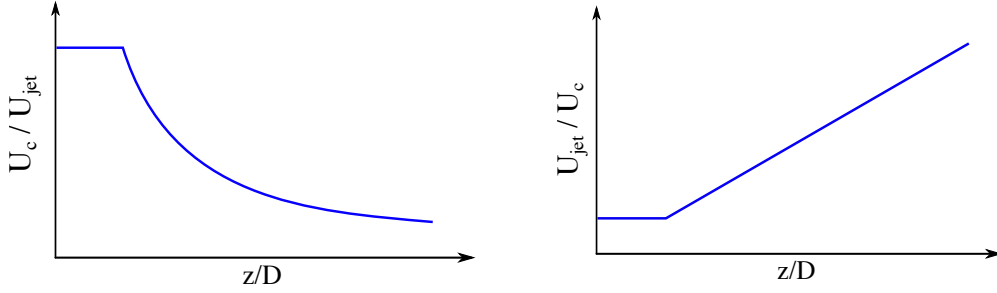


**Figure 2:** (left) Sketch of the centreline velocity as a function of axial distance and (right) the inverse of the centreline velocity as a function of axial distance.

Equation (1) can be fitted to the linear part of the inverse centreline plot to determine the decay constant,  $B_u$ , and the virtual origin,  $z_0$ .

$$\frac{U_{\text{jet}}}{U_c} = \frac{1}{B_u} \left[ \frac{z}{D} - \frac{z_0}{D} \right] \quad (1)$$

Table 1 shows values for  $z_0$  and  $B_u$  obtained from experiments by researchers.

**Table 1:** Decay constant,  $B_u$  and virtual origin,  $z_0/D$ , from experiments with turbulent round jets emerging from contraction nozzles. Table values adapted from the summary of Ball et al. [1]

Authors	$z_0/D$	$B_u$
Wyganski and Fiedler [7]	3	5.7
Hussein et al. [4]	2.7	5.9
Fellouah et al. [3]	2.5	5.59

### 1.3.2 Near-, Intermediate-, and Far Field

The flow field of a turbulent round jet can be divided into three axial regions commonly referenced as the Near Field, the Intermediate Field, and the Far Field. The three regions are sketched in Figure 1. The Near Field is the region closest to the orifice and approximately spans from  $z = 0$  to  $z = 7D$  according to the review article of Ball et al. [1]. This is also the region of the potential core for jets issuing from contraction nozzles. The potential core is not drawn in Figure 1 as the jet is emerging from an orifice in the present study. The Near Field is very important as it is in this region that the turbulence evolves from the instability in the mixing layer. The mixing layer is illustrated on Figure 1 as a wobbly dark blue line. The light blue straight line in the mixing layer represents the mean jet width. In the mixing layer an instability arises from the gradient between the energetic jet stream and the quiescent ambient fluid. Next to the Near Field lies the Intermediate Field which is more difficult to accurately define on its own and is thus best described as being neither the Near Field nor the Far Field. The axial region from  $z = 0$  to  $z = 30D$  is often referred to as the



Near-Intermediate Field or simply NIF. The Far field extends from  $z = 30D$  to the end of the jet and the flow is considered to be self-similar in this region. An effect of the self-similarity property can be seen by studying the axial velocity profile of the jet. In the Far Field, the axial velocity profiles take the form of a Gaussian function which is also sketched on Figure 1. The function is formulated as  $U/U_c = \exp(-k\eta^2)$ , where  $\eta$  is the self-similarity variable (2) and  $k$  is constant which Boersma et al. [2] determine to be  $k=76.1$ . The jet width naturally increases with downstream distance from orifice due to the entrainment of ambient fluid. However, the shape of the velocity profile does not change with downstream distance. This can be seen by plotting the velocity profile as a function of the self-similarity variable:

$$\eta = \frac{r}{z - z_0} \quad (2)$$

$r$  is the radial coordinate,  $z$  is the axial distance and  $z_0$  is the so-called virtual origin obtained from the centreline velocity decay function, equation (1). Velocity profiles measured in the Far Field region all collapse on one curve when plotted as a function of the self-similarity variable,  $\eta$ . Ball et al.[1] conservatively place the Far Field starting point at an axial distance of 30 jet diameters downstream, however, the self-similarity phenomenon can be observed much closer to the jet inlet. It has been observed that the self-similar axial profiles start to appear in the NIF at lower Reynolds number such as  $Re=2400$ . The self-similar profiles obtained by Boersma et al. [2] show excellent agreement with experiments even though the domain has a length of only 45 jet diameters.

### 1.3.3 Spreading Rate

Another important parameter in the description of the turbulent jet is the spreading rate. Quiescent ambient fluid is entrained in the jet as illustrated on Figure 1 with black arrows pointing from the surroundings into the mixing layer of the jet. Thus the mass flux of the jet increases with axial distance from orifice. However, the initial momentum supplied by the jet inlet is conserved and thus the width of the jet increases and the centreline velocity decays downstream. The spreading rate is often described with the half-radius parameter,  $r_{1/2}$ . The half-radius is simply the distance from the centreline to the radial point in which the axial velocity is half of the centreline velocity:  $U(r_{1/2})/U_c = 0.5$ . The half-radius is also shown on Figure 1. The growth of the half-radius is linear in the self-similar region. Hence, the function in equation (3) is often fitted to the axial profiles in the Far Field region.

$$\frac{r_{1/2}}{D} = A \frac{z}{D} - B \quad (3)$$

The slope of equation (3) has consistently been shown to be  $A \approx 0.1$ . Table 2 shows a few slope constants based on experimental measurements. Note that Panchapakesan and Lumley [5] do not report the intercept,  $B$ . Most likely because the measurements are performed so far away from orifice that the contribution is neglectable.

**Table 2:** Linear fit constants (equation (3)) determined from experiments with turbulent round jets emerging from contraction nozzles. Table values adapted from the summary of Ball et al.[1]

Authors	A	B
Panchapakesan and Lumley [5]	0.096	-
Fellouah et al. [3]	0.097	0.259

### 1.3.4 The Kolmogorov Length Scale

The Kolmogorov length scale is a very important parameter in any study of turbulent flows. It is especially important when attempting to perform a direct numerical simulation in which the spatial resolution should be fine enough to resolve the smallest flow structure. No flow structure smaller than the Kolmogorov length scale exists. Turbulent kinetic energy from larger flow structures break down to smaller eddies in an energy cascade until the eddies are finally dissipated as heat at the Kolmogorov length scale due to dominating viscous effects. In general, the Kolmogorov length scale is strongly dependent on Reynolds number and decreases rapidly with increased Reynolds number. For this reason, DNS simulations are usually only viable at low Reynolds number flows as the spatial resolution required for high Reynolds number flows is too computationally demanding. The exact dimension of the Kolmogorov length scale depends on the particular flow problem at hand. In the flow field of the turbulent round jet, the Kolmogorov length scale has been shown to grow with axial distance from the inlet. The Kolmogorov length scale is smallest in the Near Field region and grows linearly in the Far Field region as a function of axial distance from orifice. All equations used in the following two paragraphs can be found in Stephen B. Pope's [6] textbook on turbulent flows.

#### Far Field Kolmogorov

Boersma et al. [2] argues that the growth of the Kolmogorov length scale in the Far Field region can be expressed as  $\eta_k = 0.004z$ . Hence, the Kolmogorov length scale grows linearly as a function of the distance from orifice. Boersma et al. [2] refer to the air jet measurements of Panchapakesan and Lumley [5]. On page 213 in the referenced paper the normalized dissipation rate,  $(r_{1/2}/U_c^3)\epsilon$ , is plotted as a function of the radial coordinate. The dissipation rate is normalized with the jet half-radius,  $r_{1/2}$ , and the local centreline velocity,  $U_c$ . As result of self-similarity in the Far Field region the plot shows that the normalized dissipation rate has a constant value close to the centreline and rapidly decays with radial distance. The constant value is close to 0.017. This yields equation (4):

$$\frac{r_{1/2}}{U_c^3}\epsilon = 0.017 \quad (4)$$

The approximate relation between Kolmogorov length scale and the dissipation rate is given by equation (5):

$$\eta_k \approx \left( \frac{\nu^3}{\epsilon} \right)^{1/4} \quad (5)$$

The decay of the centreline velocity as a function of distance from orifice is obtained by the aforementioned equation (1). Combining equation (1), (4), and (5) one ends up with an approximation of the Kolmogorov length scale,  $\eta_k$ , as a function of the axial coordinate and only dependent on the Reynolds number and the decay constant,  $B_u$ . The derivation is given in full detail in appendix B.

$$\eta_k = (0.17\text{Re}^3 B_u^3)^{-1/4} z, \quad z \gg z_0 \quad (6)$$

Note that equation (6) relies on the mathematical assumption that  $z$  is big relative to  $z_0$  as the  $z_0$  term from equation (1) is dropped in order to obtain a convenient linear expression. The constant normalized dissipation rate assumption used in equation (4) is also only valid in the Far Field region as it is a result of the self-similarity phenomenon. Thus the validity of equation (6) increases with distance from orifice. Inserting  $\text{Re}=2400$  and the decay constant  $B_u$  from Boersma et al. [2], equation (6) yields:

$$\eta_k \approx 0.0012z \quad (7)$$

As mentioned at the beginning of this paragraph, Boersma et al. [2] argue that the Kolmogorov length scale is given by  $\eta_k \approx 0.004z$ , referring to the very same measurements of Panchapakesan and Lumley [5]. The source of discrepancy between Boersma's et al.'s [2] estimation of the Kolmogorov length scale and the derivation above is not clear.

### Near Field Kolmogorov

The Near Field cell size is critical as it is in this region that the Kelvin-Helmholtz instability arises which eventually leads to the jet breakup characterized by a sudden drop in centreline velocity. Hence it is important to adequately resolve this region. The main focus of Boersma et al. [2] is the Far Field region and the exact Near Field resolution is not reported. However, the cells are reported to be clustered near the orifice which is sensible as it is in this region that the smallest length scales exist. Despite the existence of numerous papers regarding the nature of various types of turbulent jets only few studies are concerned with low Reynolds number flows and the Kolmogorov length scale in the Near Field region. However, the study of Fellouah et al. [3] from 2009 investigates turbulence length scale distributions in the NIF region of round free jets at Reynolds numbers as low as  $\text{Re}=6,000$  and as high as  $\text{Re}=100,000$ . Fellouah et al. [3] have conveniently plotted the Kolmogorov length scale with respect to the axial distance from orifice in the interval  $z = 2.5D$  to  $z = 25D$ . The plot shows that the Kolmogorov length scale increases slightly from  $z = 2.5D$  to  $z = 15D$  and then grows linearly from approximately  $z = 15D$  to  $z = 25D$  as predicted by equation (6). Fellouah et al. [3] have added a straight line from  $z = 15D$  to  $z = 25D$  to mark the linear growth region, however, judging qualitatively it seems very reasonable also to use the linear relationship as close as  $8D$  from orifice as an indication of the Kolmogorov length scale magnitude. The plot from Fellouah et al. [3] can be found in appendix A.

## 2 Method

This section of the report covers the simulation setup in detail starting with the mesh construction and ending with a brief description of the post-processing method.

### 2.1 Pre-processing

#### 2.1.1 Domain

Prior to constructing the mesh, the computational domain must be determined. If one were to investigate a simple pipe flow, the interior pipe walls would define a natural domain boundary. However, in this simulation the jet is shooting from an orifice into a quiescent space and thus there are no predetermined boundaries. Hence, the computational domain must be large enough to allow for the jet to expand unrestrictedly. At the same time, one must keep the computational cost in mind. An unnecessarily large domain is costly and should be avoided. The size of the domain is thus determined based on general theory of turbulent jets. The computational domain is shown in Figure 3.

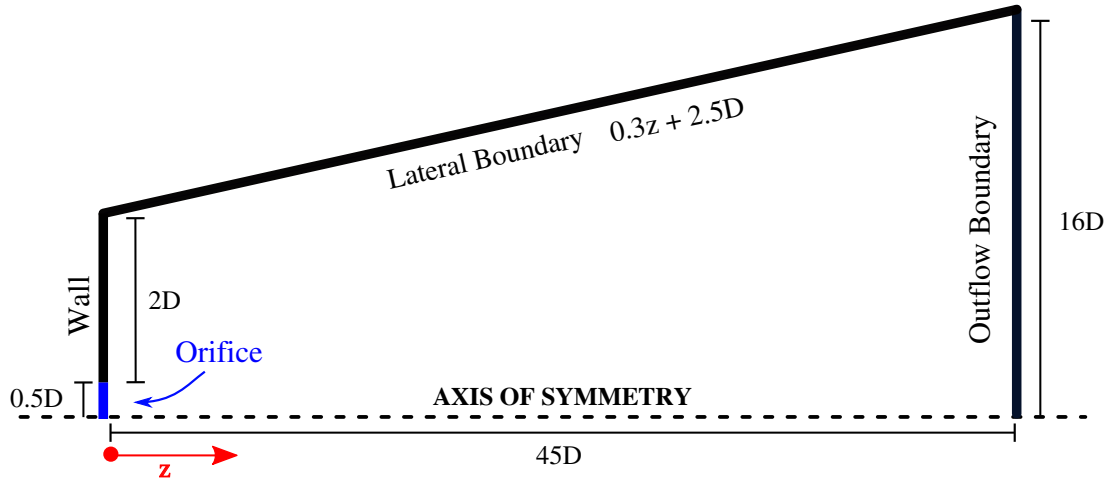


**Figure 3:** Half-cross-sectional view of the conical computational domain. The illustration shows the domain boundaries with dimensions. Note that the expression  $0.3z + 2.5D$  is the radial distance of the lateral boundary as a function of axial distance from orifice.

As described in the theory section the jet can be divided into three regions: Near-, Intermediate-, and Far Field. The jet expansion is greatest in the self-similar Far Field region and the expansion rate based on the jet half-radius is linear. Thus, a conical domain following the Far Field expansion rate is a sensible choice. The jet half-radius is roughly given by the relation  $r_{\frac{1}{2}} = 0.1z$ . The jet half-width is roughly two times the half-radius. In order to obtain a reliable solution some distance between the jet and the domain boundary is preferred. Hence, the lateral domain boundary is chosen to

expand at three times the rate of the jet half-radius. Two diameters of padding is also added to put some distance between jet and lateral boundary near the orifice. Thus, the radius of the lateral boundary is given by the function  $0.3z + 2.5D$ .

### 2.1.2 Gmsh

The mesh is created in Gmsh which is an open source mesh generator released under the GNU General Public License (GPL). Gmsh is marketed as three-dimensional finite element mesh generator and includes numerous tools for creating unstructured grids. However, Gmsh is also capable of generating simple structured grids though the degree of control is quite limited. Gmsh deals with two types of file formats: '.geo' and '.msh'. The '.geo' file is a simple text file which stores information about points, lines, surfaces, boundaries, and also defines how Gmsh generates the final mesh. Thus grids can be build using the graphical user interface (GUI) and by entering commands in the the '.geo' file. It is easiest to sketch the desired domain in the GUI and modify mesh control parameters in the text file. This method is especially powerful when working with a fine mesh such as the one used in the this study as the mesh can be modified without the need to view it in the GUI. Based on the '.geo' file, Gmsh exports a generic '.msh' file which can be easily be converted to the OpenFOAM mesh format in the OpenFOAM command line interface.

### 2.1.3 Mesh Design

#### Cell Size

As this is a direct numerical simulation, grid resolution must be considered carefully. A true DNS simulation spatially resolves the flow down to the Kolmogorov length scale which is denoted  $\eta_k$  in this report. Having decided on the domain dimensions and equipped with a reasonable estimate of the Kolmogorov length scale from the General Theory section, the actual mesh had to be designed. It was chosen to use an O-grid which is a structured grid well-suited for cylindrical geometries. The frame of the grid in the inlet plane is shown in Figure 4. The cells are constructed in Gmsh based on the so-called Transfinite Line Algorithm. One specifies the desired number of cells on a specific frame line which is used as boundary conditions for the algorithm when creating the three-dimensional structured grid. The square is found at the very center of the grid and the diagonal length is  $0.6D$ . The square size relative to the orifice size is a compromise. All the blue arcs on Figure 4 must be divided into an equal number of segments. Thus, a small square would lead to a large cell size ratio between cells at the grid center and cells near the edge of the orifice. Making the square too big leads to highly skewed cells between the square sides and the orifice edge and the asymmetric square could also have an non-physical effect on the flow field. The square sides are curved slightly so that cells between the square and the outer orifice ring become less skewed. The width and height of the cells are controlled by the cell density on the blue arcs and the green lines respectively (Figure 4). The arcs and lines are divided into a number of uniformly spaced segments required to achieve the desired cell size in the inlet plane. Hence, the cells inside the orifice have approximately the same size. It is noteworthy, that the circumferential length increases with radial distance from origo

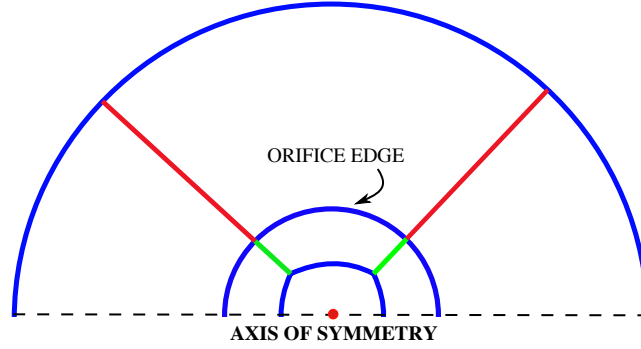


**Figure 4:** Illustration of mesh frame controlling the grid in the inlet plane. The red dot represents origo. The blue arcs control the circumferential cell dimension (cell width). The green and red line controls the grid size in the radial direction (height).

so the cells naturally become wider outside the square. However, the spatial resolution matters less further away from the jet and it is thus an acceptable side effect. The cell width and height also increase with axial distance from orifice due to the expanding nature of the conical domain geometry. This effect is also acceptable as the Kolmogorov length scale increases downstream. The red lines on Figure 4 control the cell height outside orifice. The cells are not uniformly spaced on the red line. A small amount of stretch is added so that the cell height increases as a function of radial distance from the centreline. This lowers the total number of cells in the mesh without sacrificing spatial resolution in the jet.

The mesh is divided into two sections in the axial direction. As mentioned in the General Theory section, the linear growth of the Kolmogorov length scale in the Far Field also gives a reasonable estimate of the Kolmogorov length scale as close as  $z/D=8$ . It is then assumed that the length scale at  $z/D=8$  is representative in the region  $z/D=0$  to  $z/D=8$ . Thus the cell length,  $\delta z$ , is constant in the first section. In the General Theory section it was deduced that the Kolmogorov growth was given by  $\eta_k = 0.0012z$ , though Boersma et al. [2] state that it is given by  $\eta_k = 0.004z$ . It was chosen to use a coarse mesh, DNS1, with a Near Field cell size of  $0.1D$  for the first simulations which is about three times bigger than Boersma et al.'s [2] equation predicts. The need for grid refinement was thus expected. In the second section from  $z = 8D$  to  $z = 45D$ , a small amount of axial stretch is applied to the cells downstream to represent the growth of the Kolmogorov length scale. The Kolmogorov length scales grows linearly as described in the General Theory section, however, the stretching method in Gmsh is limited to a cell-to-cell progression. The user specifies the ratio between consecutive cells on a line. This effectively means that the cell length grows exponentially as a function of axial distance from orifice. The progression was specified such that the cell length at the domain end,  $z = 45D$ , did not exceed  $0.004 \cdot 45D = 0.18D$ . Figure 5 shows the orifice patch and a half-cross-sectional view of the DNS2 mesh to give a visual impression of the grid.

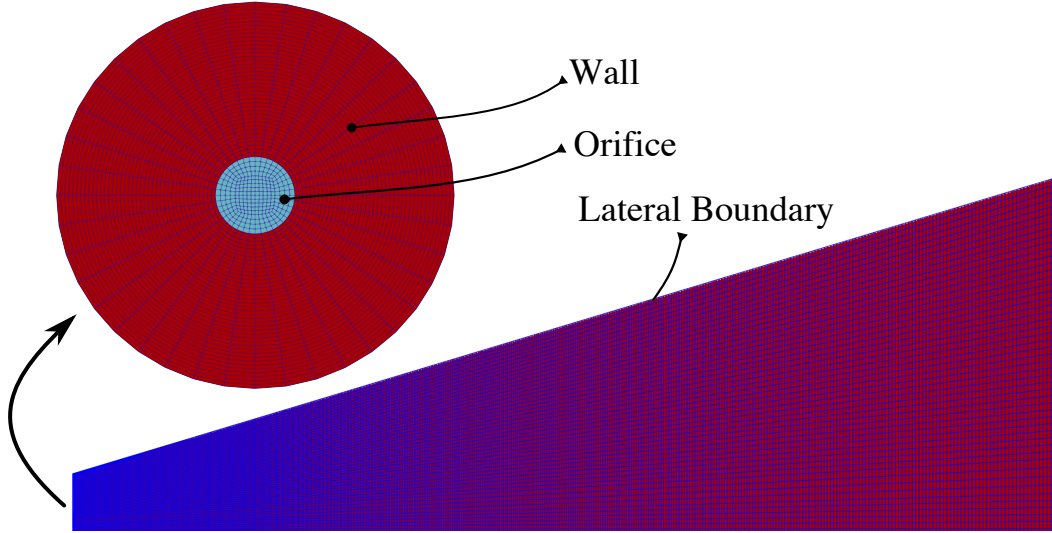


**Figure 5:** Two different angles of the DNS2 mesh extracted from ParaView. The image shows the orifice patch in turquoise bounded by the wall patch in red. The figure also shows the half-cross-sectional view of the mesh. The grid lines are blue and the cells are red which gives a visual indication of the cell density in the domain. The axial cell growth is confirmed smooth though ParaView’s faulty rendering showing blue vertical stripes gives the impression of mesh imperfections.

### Mesh Specifications

The Results section presents data from primarily three different grids denoted: 1, 2, and 3. Hence, the DNS1 simulation is a direct numerical simulation performed with mesh 1. Mesh 1 is the coarsest mesh and mesh 3 is the finest mesh. The mesh specifications are given in Table 3 below. The table shows the constant axial cell dimension from  $z = 0$  to  $z = 8D$ , the axial stretch of cells in the region  $z = 8D$  to  $z = 45D$ , the axial cell dimension at the outflow boundary, the radial cell stretch outside the orifice block, and the total number of cells.

**Table 3:** Mesh specifications of the three different grids that were used for the simulations.

Mesh	$\delta z$ (0 to 8D)	Axial Stretch (8D to 45D)	Outflow $\delta z$	Radial Stretch	Cells
1	0.1D	0.2%	0.174D	-	166005
2	0.05D	0.35%	0.18D	-	978,360
3	0.025D	0.4%	0.174D	1%	3,900,225



## 2.2 Simulation Configuration

### 2.2.1 OpenFOAM

The simulation is carried out in OpenFOAM v4.1 which is an open source software released under GPL. OpenFOAM is essentially a C++ toolbox for computational mechanics, primarily focused on CFD using the finite volume method. OpenFOAM is also equipped with meshing tools and some post-processing utilities. OpenFOAM is a native Linux application and is controlled from the terminal and by manipulating text files. OpenFOAM has extensive CFD capabilities, however, the lack of documentation and graphical user interface creates a steep learning curve.

### 2.2.2 Governing Equations

OpenFOAM includes a wide range of numerical algorithms to pick from when solving a particular flow problem. This study investigates a low Reynolds number turbulent jet and the flow is thus governed by Navier-Stokes equations in incompressible form as well as the continuity equation:

$$\frac{\partial \mathbf{u}}{\partial t} + \nabla \cdot (\mathbf{u}\mathbf{u}) = -\frac{1}{\rho}\nabla p + \nu\nabla^2 \mathbf{u} \quad (\text{momentum}) \quad (8)$$

$$\nabla \cdot \mathbf{u} = 0 \quad (\text{mass}) \quad (9)$$

$\mathbf{u}$  denotes the three-component velocity vector and  $p$  denotes the pressure. Both density,  $\rho$ , and the kinematic viscosity,  $\nu$ , are assumed to be constant.

### 2.2.3 Numerical Method

It was considered at first to use the OpenFOAM solver `dnsFoam` to solve the momentum and mass conservation equations as the name of the algorithm seemed suitable for a DNS simulation. However, a closer inspection of `dnsFoam` reveals that it relies on the well-known PISO algorithm and that the solver includes a small random body force term. The body force term is designed to keep the turbulence alive in the `boxTurb` tutorial case with as cyclic boundary conditions as the turbulence would otherwise die out over time when slowly dissipated as heat. In the study of the turbulent jet, the turbulence should be kept alive by the existence of mean velocity gradients and hence no body force is needed. It was then decided to use the OpenFOAM solver `pisoFoam` which is a transient solver for incompressible turbulent flows based on the PISO algorithm. The fluid is specified as 'Newtonian' and in the case of the DNS simulation, the turbulence model is specified as 'Laminar' which simply means that no turbulence modelling is used. The turbulence model used for the LES simulation is called `dynamicKEqn` in OpenFoam and it is a local dynamic one-equation eddy viscosity model.

Temporal discretization is done with a second order accurate Backward time scheme, the spatial discretization is performed with the second order accurate Gauss Linear



scheme, and the interpolation scheme is linear. The convergence criteria at each time step is determined by specifying the relative tolerance and absolute tolerance of the residuals. The relative tolerance criteria is set to zero for both velocity field and pressure field to force the solution to converge to the absolute tolerance in each time step. The absolute residual tolerance is set to  $10^{-5}$  for the velocity field and  $10^{-6}$  for the pressure field. All simulations were performed on the Niflheim cluster supercomputer belonging to the Department of Physics at DTU. The domain was decomposed into 16 roughly equal subdomains and run in parallel on a 16-CPU node with 64 GB RAM.

#### 2.2.4 Boundary Conditions

This sections describes the boundary conditions used in the simulations. The computational domains is bounded by four boundaries: orifice, wall, lateral, outflow. The boundaries are marked on the domain illustration Figure 3.

**Inlet BC - Uniform** At the orifice inlet a uniform velocity profile is used to emulate the flat profile produced by the ideal jet. This is the inlet velocity profile that Boersma et al. [2] use in their simulation. In the present study the inlet velocity is set to  $U_{\text{jet}} = 1\text{D/s}$ . The pressure is left free at the inlet.

**Inlet BC - Contraction Profile** The uniform inlet velocity profile introduces and infinite gradient when being bounded by a no-slip wall condition. Infinite gradients are not physical and even though it is standard practice to use the uniform profile an alternative inlet velocity profile was investigated as well. The alternative velocity profile has a more realistic velocity drop near the edge of orifice thus smoothing the aforementioned gradient between the jet inlet and the no-slip wall condition. The alternative velocity profile is plotted along with the uniform profile in Figure 6 which also shows a 3D illustration of this velocity profile.

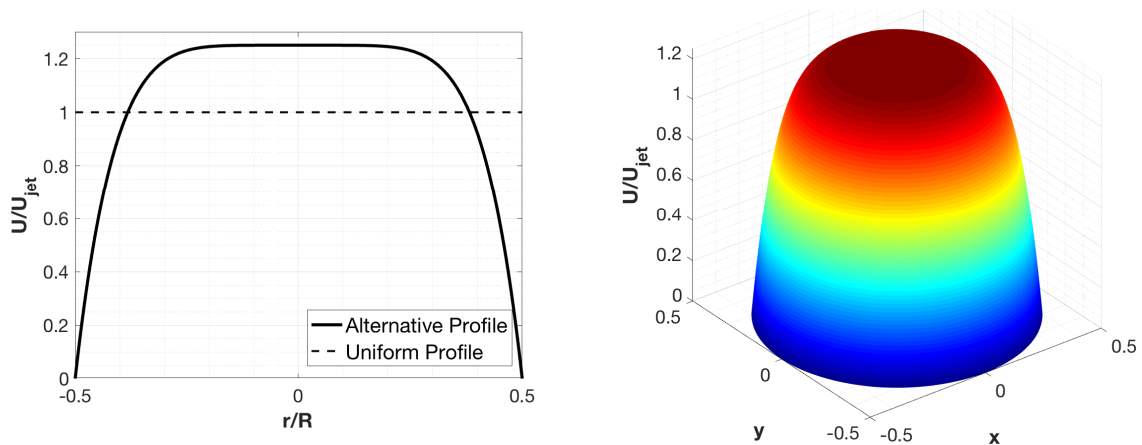


**Figure 6:** (left) 2D-plot of the alternative profile along with the uniform profile for reference. (right) 3D-plot of the alternative profile.

The alternative inlet velocity profile is given by equation (10):

$$U(r) = U_{\text{ref}} \left[ 1 - \left( \frac{r}{R} \right)^n \right] \quad (10)$$

The parameter  $n$  dictates the curvature of the profile. The constant  $U_{\text{ref}}$  adjusts the peak velocity such that the momentum flux of the alternative profile is equivalent to that of the uniform profile. In appendix C it is shown that  $U_{\text{ref}}$  is given by equation (11):

$$U_{\text{ref}} = U_{\text{jet}} \sqrt{\frac{\int_0^R r dr}{\int_0^R r \left[ 1 - \left( \frac{r}{R} \right)^n \right]^2 dr}} \quad (11)$$

Defining  $n = 2$  yields a parabolic profile and not a top-hat profile. High numbers of  $n$  results in steep gradients near the edge of the orifice. As the orifice consists of a finite number of cells, too high of a gradient would not be resolved well on the grid when implemented in OpenFOAM. As a compromise it was chosen to use  $n=6$  which gives  $U_{\text{ref}} \approx 1.25$ . The implementation is visualized in Figure 7 which shows the inlet plane of the mesh with the orifice in the middle surrounded by the wall boundary. The cells are color-coded according to velocity magnitude. This velocity profile is denoted the 'contraction profile' in the Results and Discussion section as it emulates the velocity profile of a strong contraction nozzle.

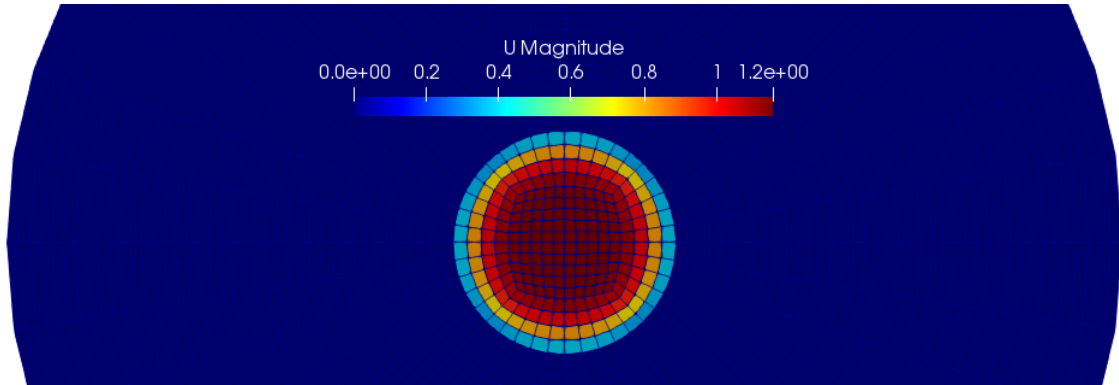


**Figure 7:** The implementation of the contraction velocity profile in OpenFOAM. The image shows the wall and orifice boundary patches of the DNS2 mesh, color-coded according to velocity magnitude.

### Inlet BC- Noise

The report of Boersma et al. [2] does not mention inlet turbulence modelling. However, it was seemingly not possible to attain the desired instability and transition to turbulence without inlet noise. Evidence of this is provided in the Results and Discussion section. Thus a uniform profile with noise in the form of minor uncorrelated fluctuations was investigated in addition the uniform profile and the alternative profile.

### Wall BC

A conventional no-slip boundary condition which specifies zero velocity is applied to the wall patch. The pressure is left free.

### Lateral BC

The lateral boundary condition must allow for the entrainment of ambient fluid in order to represent the physics. Section 5.2.3.2 in the OpenFOAM 4.1 User Guide covers the so-called entrainment boundary condition. It is recommended by the User Guide to use a combination of the totalPressure pressure boundary condition and the so-called pressureInletOutletVelocity velocity boundary condition. The totalPressure boundary conditions is defined as:

$$p = \begin{cases} p_0 & \text{for outflow} \\ p_0 - \frac{1}{2}U^2 & \text{for inflow (incompressible, subsonic)} \end{cases}$$

The user specifies  $p_0$  which in this case is set to zero. In the pressureInletOutletVelocity velocity boundary condition, the velocity is left free at all times except for the inflow where the tangential component is set to zero. Thus it is a standard pressure boundary condition with unspecified velocity when fluid is flowing out of the domain, however, unstable velocity spikes are moderated when fluid flows into the domain according to the OpenFOAM User Guide. The fluid inflow velocity at the lateral boundary is quite small and it would most likely be stable to use a standard pressure boundary condition. Nevertheless, the totalPressure and the pressureInletOutletVelocity boundary conditions were applied to the lateral boundary.

### Outflow BC

The outflow patch was first equipped with a pressure boundary condition in which the pressure was set to zero and the velocity was left free. However, this boundary condition proved to be unstable. Figure 8 shows the outflow boundary of a simulation not long before the simulation crashed.

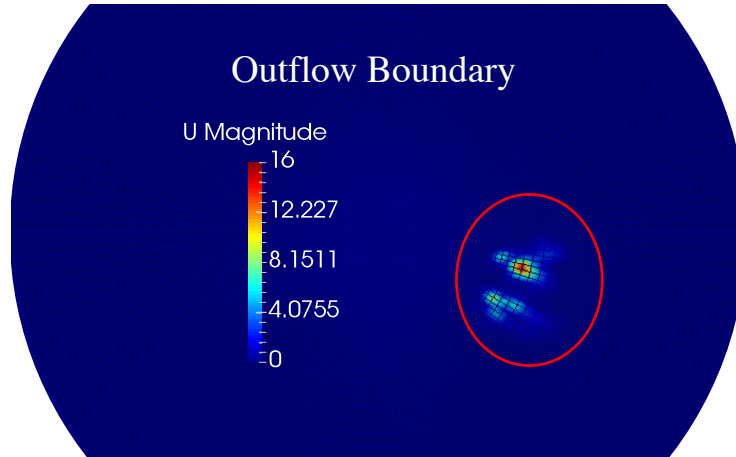


**Figure 8:** Image showing the outflow boundary not long before a simulation with the unstable outflow boundary condition crashed. The instability is marked by a red circle.

The velocity spike of 16D/s leading to the crash is marked by a red ellipse on Figure 8. The color-coding is scaled to the visible range and thus it is not possible to see the bulk outflow as it has velocity magnitude of around 0.2D/s. The stability issue

on the outflow boundary condition was redeemed by adopting the boundary condition of the lateral boundary. Thus the outflow patch also uses the totalPressure and the pressureInletOutletVelocity boundary conditions described in the paragraph above.

### 2.2.5 Initial Condition

Turbulence will not develop by itself. In real life small flow field disturbances exist even in seemingly absolute still rooms. These small disturbances trigger the development of larger turbulent velocity fluctuations. From a modelling perspective, this means that an initial condition specifying the internal field as zero velocity does not adequately capture the physical nature of the problem. Simulating a perfectly turbulence free inlet shooting into a perfectly still room would simply result in a non-developing uniform jet. Hence some artificial disturbance must be introduced to produce the turbulent jet.

According to the paper of Boersma's et al. [2] the simulation is started from a non-uniform initial field condition consisting of small velocity fluctuations with an amplitude of  $0.001U_{\text{jet}}$ . The report does not mention any inlet turbulence modelling and thus it is assumed that Boersma et al. [2] only used the reported initial perturbation to trigger the turbulence and that the turbulence was kept alive by the instability in the shear layer. Following this example, correlated velocity perturbations in the order of  $0.01U_{\text{jet}}$  are used as an initial condition in my simulation. The perturbations are produced by interpolating velocities from the initial condition of OpenFOAM's tutorial case named boxTurb on to the initial field of my simulation. BoxTurb is essentially a tutorial case modelling a box of turbulence with cyclic boundary conditions solved with the dnsFoam algorithm. boxTurb comes with an utility for creating the initial velocity field which is controlled by a few parameters related to the turbulence kinetic energy in the flow. The utility was exploited by modifying the box shaped mesh of the tutorial case such that it was large enough to enclose the jet mesh. The parameters were then manipulated until the velocity magnitude reached the aforementioned value and mapped on to the initial velocity field of the jet simulations using the mapFields OpenFOAM command.

### 2.2.6 Temporal Resolution

In order to run the simulation a central time parameter must be set: the time step  $\delta t$ . Most OpenFOAM solvers require the local Courant number to be less or equal to 1 to achieve numerical stability. However, as this is transient study, temporal accuracy must also be considered and thus aiming for a Courant number of 1 might not be accurate enough. To reduce the computational cost, the time step is preferably as large as possibly without compromising temporal accuracy. The Courant number for one cell in one dimension is given by:

$$Co = \frac{\delta t |U_z|}{\delta z} \quad (12)$$

$U_z$  is the local fluid velocity and  $\delta z$  is the cell size in the flow direction. It is only necessary to consider the axial direction as this is by far the dominating velocity component. The highest Courant numbers occur near the orifice in the present study as

this region has a combination of high velocities from the inlet and small cells to resolve the Kolmogorov length scale. The time step used for the simulations were dependent on the grid. The time step,  $\delta t$ , was conservatively specified such that the global maximum Courant number would be approximately  $Co = 0.5$ . The global average Courant number is much smaller with a value of approximately  $Co = 0.004$  for all simulations.

## 2.3 Post-processing

### Sampling

Post-processing was carried out in ParaView, MATLAB, and with the inbuild OpenFoam postProcessing utility. ParaView was mainly used for visualization of the jet. The plots presented in the Results section are sampled with OpenFoam's CLI (Command Line Interface) postProcessing utility named singleGraph. High resolution line sources with 1000 uniformly distributed points were used to sample data from the velocity field and then processed in MATLAB. Unless otherwise specified in the Results section, the simulations were run for  $300 D/U_{jet}$  timescales and data was saved every fifth timescale. Mean values were obtained by averaging from 200 to 300 timescales as it was assumed that at least the centreline velocity would be fairly statistically stationary after 200 time scales. One can assume that the centreline velocity almost does not decay for the first 10 jet diameters,  $U_c/U_{jet} \approx 1$ , as the results of Boersma et al. [2] suggest and the centreline velocity from  $z = 10D$  to  $z = 45D$  is accurately described by equation (1). Hence, it can be shown that the transit time from orifice to the end of the domain at the centreline is roughly 100 timescales. Thus, flow structures as convected at as low as 50% of the centreline velocity should have reached the end of the domain after 200 timescales. This rough estimate proved reasonable when simulating.

### Validation Data

The simulation results are compared with the mean flow statistics of Boersma et al. [2]. The data from Boersma et al. [2] is not directly available. Hence, the open source program Plot Digitizer was used to convert the figures from Boersma et al.'s [2] article to data points which could then be plotted in MATLAB together with the results of the present study.

### 3 Results and Discussion

This section of the report presents the most important findings of the present study starting with the direct numerical simulation and ending with the large eddy simulation.

#### 3.1 DNS

The jet was first simulated with the 166,005 cell mesh, DNS1. Consult the Mesh section for specific grid details. The centreline velocity was used as initial validation against the results of Boersma et al. [2]. The DNS1 results were promising as seen on Figure 9 below:

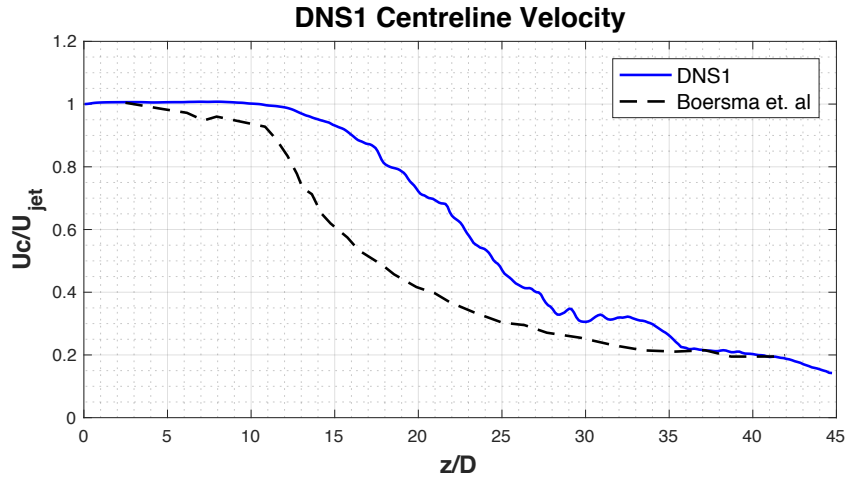


**Figure 9:** Plot of the centerline velocity as function of axial distance from orifice. The results are obtained with the DNS1 mesh and plotted along with results of Boersma et al. [2]

Though the results of the DNS1 simulation do not match those of the Boersma et al. [2], the general trend of the curve is reasonable. The jet clearly has a break up point and the velocity at the end of the domain fits well. Note here that Boersma et. al [2] do not present results of the last 2.5 diameters of the domain ( $z = 42.5D$  to  $z = 45D$ ) as they argue that the results were disturbed by the outflow boundary. The mesh was then refined near the orifice to better resolve the turbulence. As described in the Mesh section, refinement was expected. However, surprisingly, the jet break up point did not move closer to the orifice inlet as the mesh was refined. Successive grid refinements all resulted in simulations approaching more laminar solutions over time. The jet was clearly unstable and turbulent upon entry in the domain. However, the break up point of the jet was moving further away from orifice with time, the centreline fluctuations were being damped over time, and it was quite clear from visual inspection of the velocity field that the jet was approaching a non-physical laminar solution. Figure 10 shows the velocity field of the DNS2 simulation with approximately 1 million cells. The snapshot of time  $T=25s$  clearly shows the instability caused by the initial perturbation as the jet enters the domain. The simulation was run for a total of 900 timescales, far

beyond the point of which the jet converged in time. The snapshot at time  $T=900s$  shows the laminar behavior of the jet.

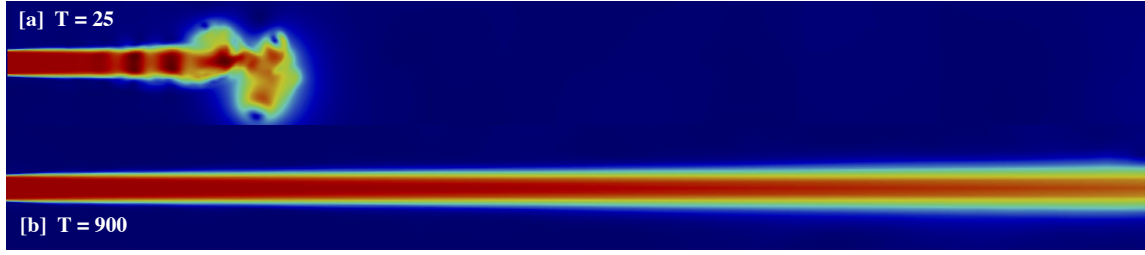


**Figure 10:** The velocity field of the jet obtained with the DNS2 mesh at time  $T=25s$  and  $T=900s$ . The turbulence seen at  $T=25s$  dies out and the jet clearly approaches a laminar solution over time.

Figure 11 shows the mean centreline velocity averaged over 20 measurements from  $T=200$  to  $T=300$  timescales. The instantaneous centreline velocity at  $T=900s$  which corresponds to snapshot [b] in Figure 10 is also plotted as well as the results of Boersma et al. [2] for reference. Comparing with the much coarser mesh, DNS1, plotted in Figure 9, the jet break up point has moved much further out and the lack of fluctuations in the  $T=900s$  instantaneous centreline velocity indicates that the jet has settled on a laminar-like flow field.

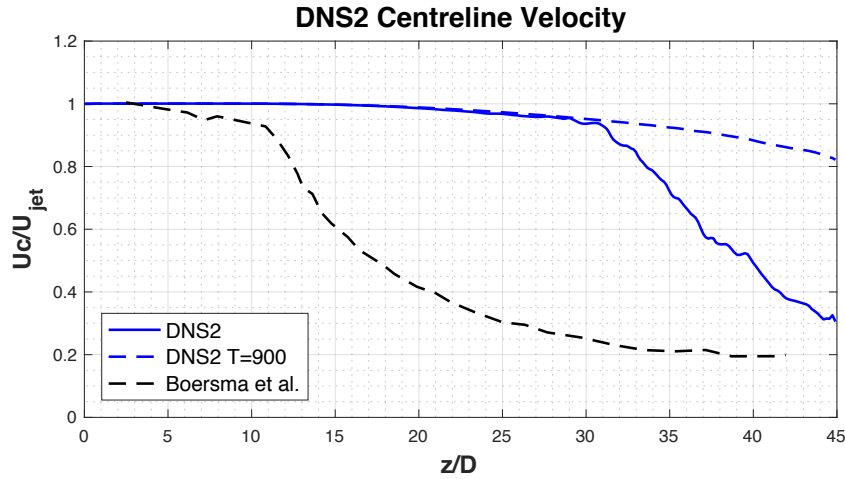


**Figure 11:** Centreline velocity plot of the DNS2 simulation. The mean centreline velocity averaged over 20 samples from  $T=200$  s to  $T=300$  s breaks up much further into the domain than expected. The instantaneous centreline velocity at  $T=900s$  shows that the turbulence has died out and the jet has settled on a laminar solution.

The laminar outcome is interesting in regard to the so-called natural transition to turbulence. Boersma et al. [2] specifically state that a forced transition to turbulence would invalidate their study of universal self-similarity in the flow field of the turbulent round jet and hence no inlet noise is used. I am not gonna dispute the fact that Boersma et al. [2] did achieve turbulent transition only using an initial velocity perturbation at a Reynolds number of 2400. However, I do find it surprising that I was unable to replicate this behavior. I have only included graphs and images from the DNS2 simulation

leading to a laminar-like flow field. However, in the persistent attempt not to force the turbulent transition, I performed multiple grid refinements which all showed the same tendency. In fact, the image of the unstable outflow boundary condition shown in Figure 8 is actually from a 10 million cell mesh with an approximate cell size of  $0.01D$  near orifice. It must be noted though, that the time step used in that particular simulation was less conservative and specified such that the maximum global Courant number would be approximately 1. The computational task of solving the 10 million mesh was quite demanding which is why the attempt to achieve natural transition with the contraction profile was introduced.

### Contraction Profile

The contraction profile is described in detail in the Boundary Condition section. The plot in Figure 12 shows the result of this simulation.

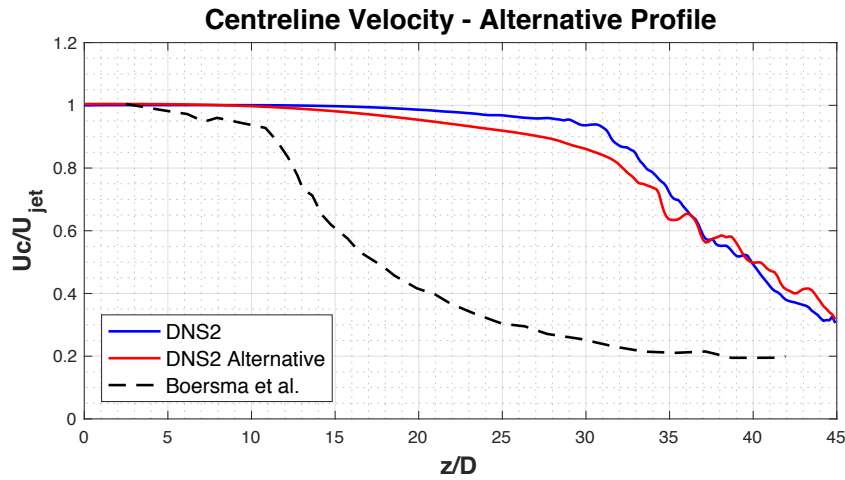


**Figure 12:** Comparison of the contraction profile, DNS2 Alternative, and the uniform inlet profile, DNS2. The profiles do produce different results when averaging 20 samples between 200 and 300 timescales. However, both profiles lack the desired fluctuations indicating instabilities.

The profiles clearly produce different results. The contraction profile does not have a clear break up point and the fluctuations, which is a sign of turbulent behavior, are being flushed out of the domain. Simulating the contraction profile for a longer time revealed that it was simply approaching the laminar-like flow field faster than the flat velocity profile. This is somewhat consistent with the results of Boersma et al. [2] as they report that a parabolic velocity profile did not transition at the given Reynolds number. Thus, it was decided to add a small amount of inlet noise to trigger the turbulence.



## Inlet Noise

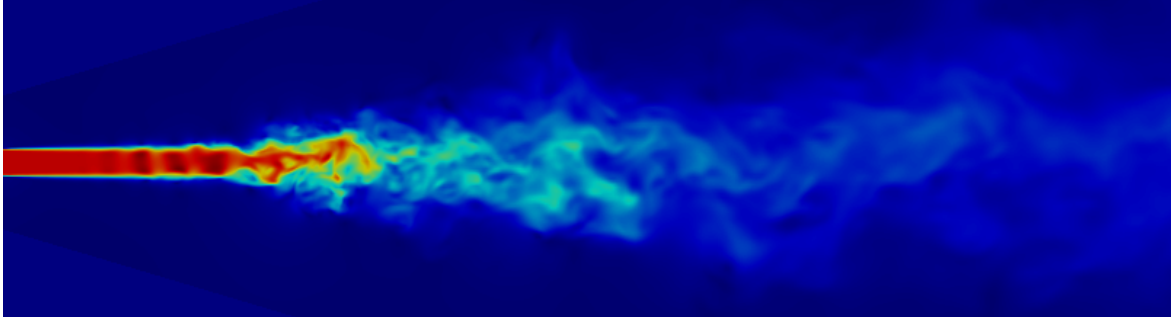


**Figure 13:** Instantaneous velocity field of the DNS3 simulation at  $T=1000$  timescales. Color-coded according to velocity magnitude.

Inlet noise in the form of minor fluctuations were superimposed on the uniform velocity profile. The fluctuations were applied to all three velocity components. Fluctuations of 1% of  $U_{\text{jet}}$  were first attempted with great success. The break up point of the jet was stable and situated five diameters from orifice. The inlet noise was then reduced by 1/10 three consecutive times. Inlet noise of 0.001% started to resemble the simulations without noise and hence this was the lowest noise level attempted. A comparison between the different noise levels is shown in Figure 14.

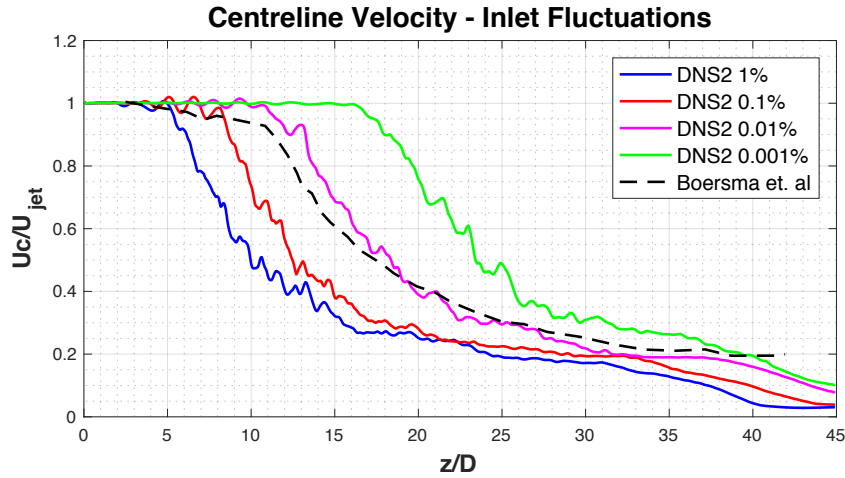


**Figure 14:** Centreline Velocities of different inlet noise levels. The fluctuation percentage which is applied to all three velocity components at the inlet can be seen in the plot legend.

The centreline velocity decay produced by an inlet noise of 0.01% lies fairly close the results of Boersma et al. [2]. This particular number is quite interesting as the turbulence intensity at the nozzle outlet in the experiment by Panchapakesan and Lumley [5] is reported to be in the order of 0.01% as well. It was then chosen to continue with 0.01% noise and refine the grid to approximately 4 million cells, grid number 3, with a constant axial grid dimension in the Near Field of  $\delta z = 0.025D$  as specified in the Mesh section. DNS3 was initially run for 300 timescales. Time histories

were sampled during run-time with probes placed on the centreline. Judging by the time history near the domain end,  $z = 40D$ , stationarity at the domain end had just barely been achieved at this point in time (Figure 15). Thus, it was decided to prolong the simulation for a total of 1000 timescales.

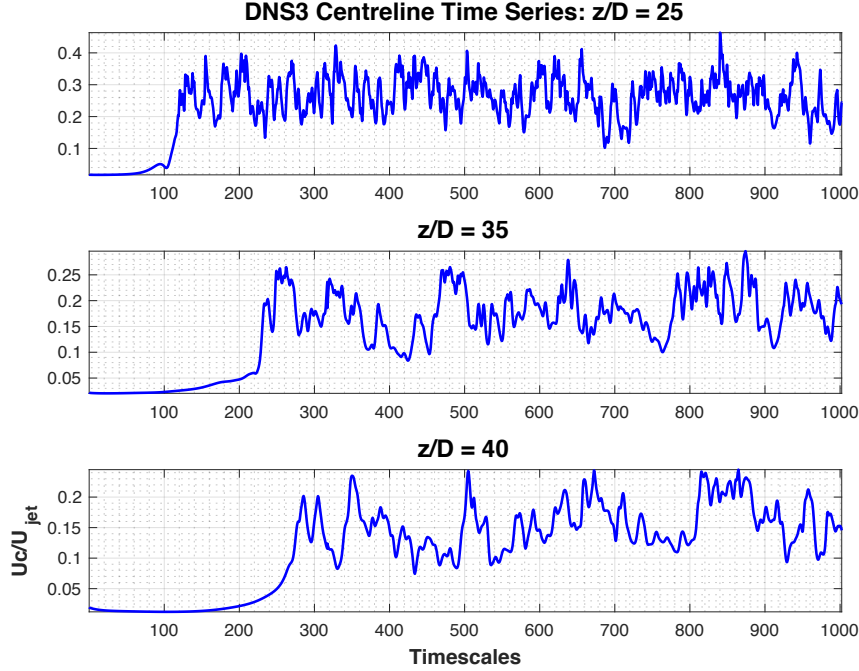


**Figure 15:** Time history from the DNS3 simulation sampled from probes on the centreline at  $z/D=25, 35$ , and  $40$ .

The mean centreline velocity as a function of axial distance obtained from the DNS3 simulation is shown in Figure 16. It is the mean values of 120 measurements equally spaced in time between  $T=400$  and  $T=1000$  timescales. The DNS3 jet breaks up earlier than that of Boersma et al. [2] which makes sense as DNS3 has inlet noise. It is also noteworthy that the DNS3 jet has a lower centreline velocity near the end of the domain. This could indicate that the Far Field region is spatially under-resolved.

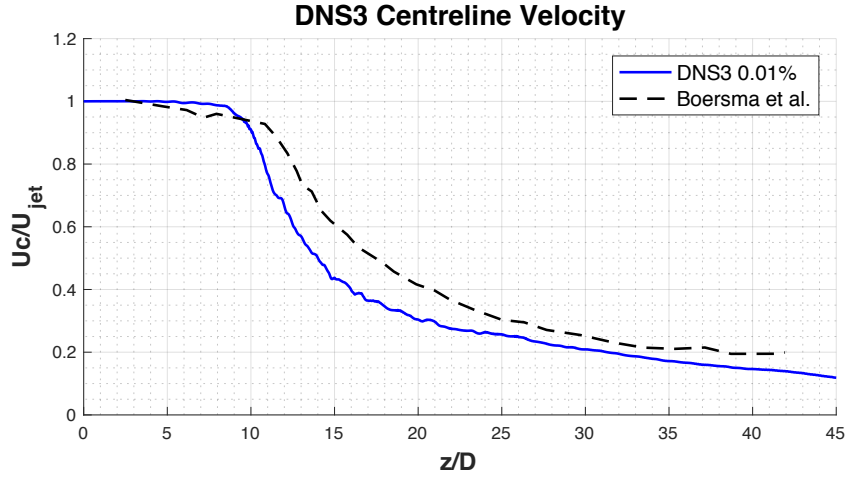


**Figure 16:** Centreline velocity of the DNS3 simulation compared with the results of Boersma et al. [2].

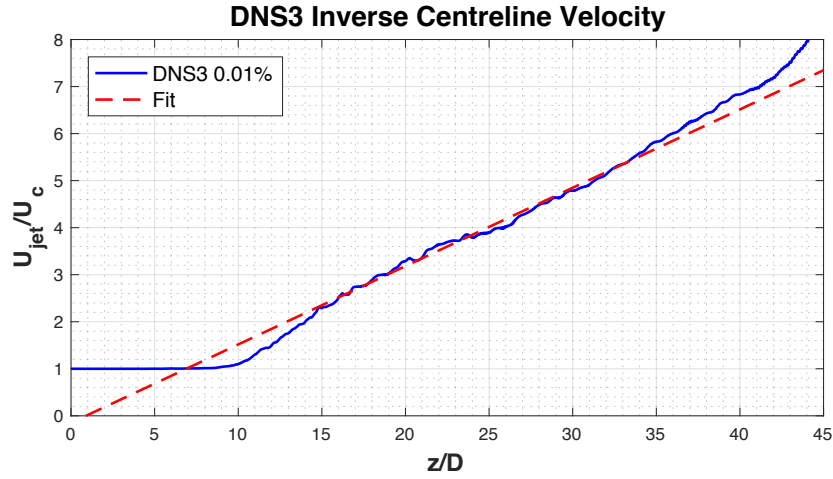


**Figure 17:** The inverse centreline velocity of the DNS3 simulation plotted along with the respective linear fit.

The inverse centreline velocity is plotted in Figure 17 and the decay function (1) is fitted to the linear part from  $z/D = 15$  to  $z/D = 35$ . This yields a decay constant of  $B_u = 6$  and a virtual origin of  $z_0/D = 0.9$ . The decay constant fits well with the experimental values presented in the General Theory section as  $B_u$  is generally between 5 and 6. The virtual origin is quite low compared to the experimental values which is an effect of the inlet noise leading to an early break up point of the jet.

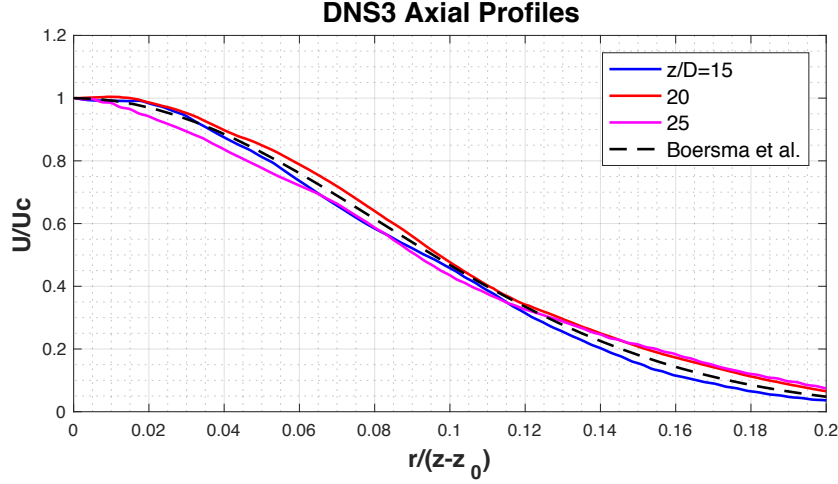


**Figure 18:** Axial velocity profiles at  $z/D=15$ , 20, and 25 plotted along with the Gaussian fit from Boersma et al. [2] for comparison.

The axial velocity profiles were then computed (Figure 18). The profiles are normalized with the axial coordinate and the virtual origin such that they ideally collapse to one curve as described in the General Theory section. Profiles 15D, 20D, and 25D of axial distance from orifice are plotted along with the Gaussian fit,  $U/U_c = \exp(-76.1\eta^2)$ , from Boersma et al. [2] in Figure 18. The axial profiles agree very well the results of Boersma et al. [2] up to  $z/D = 25$ . However, further into the domain, the profiles start to deviate slightly. Figure 19 shows the axial profile at  $z/D = 35$ .

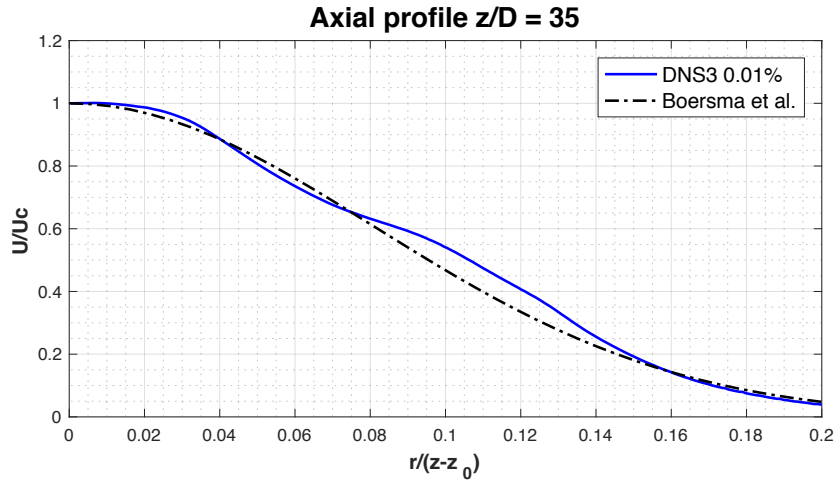


**Figure 19:** Axial velocity profiles at  $z/D=35$  plotted with Boersma et al.'s [2] Gaussian fit for comparison.

The profile at  $z/D = 35$  seems less statistically converged than the profiles closer to orifice. I attribute this effect partly to the possibly insufficient spatial resolution in the Far Field, however, it is definitely also an effect of the sampling technique. I found no convenient way to average circumferentially and my spatial averaging is based on

samples from two perpendicular radial lines. Being able to average circumferentially in the domain would lead to far better overall convergence. This is especially true near the end of the domain with few independent samples. I estimated the integral time scale based on integration of the Autocorrelation Function (ACF) of the previously shown time series at  $z/D = 35$  (Figure 15) to be approximately 8.7 timescales at the centreline at  $z/D=35$ . Thus, not all samples are independent (sampling frequency of  $1/5$  timescales) in the Far Field because the integral length scale grows and the velocity decays.

Key parameters from the DNS3 simulation are summarized in Table 4. The mean statistics of the DNS3 simulation correspond well to those of experimental researchers (General Theory section) and Boersma et al. [2]. However, the small time step and the large number of cells made the computation rather expensive. The 1000 timescales of simulation take approximately 70 hours to complete with the computing power presented in the Numerical Method section. The same number of timescales take approximately 9 hours to complete with the DNS2 mesh. It must be noted here that much less simulation time is needed if one takes advantage of the rotational symmetry and manages to average circumferentially. Nevertheless, the computational cost drastically increase with Reynolds number and the scope of simulating a Reynolds number of  $Re = 20,000$  would be very demanding with DNS. Hence, the LES simulation was initiated to investigate whether results as promising as the DNS3 simulation could be achieved with the less computational power.

### 3.2 LES

The LES simulation is based on the dynamicKEqn model in which the turbulence kinetic energy equation is solved based on coefficients derived from local flow properties. The mesh used is the 1 million mesh just like the DNS2 simulations. The total simulation time is also 1000 timescales, with a sampling frequency of  $1/5$  timescales. Mean values are obtained by averaging from 400 to 1000 timescales. At first, the regular uniform inlet profile was used. Consistent with the DNS simulations, natural transition to turbulence did not occur. Hence, inlet noise of 0.01% is used for all results presented in the plots below.

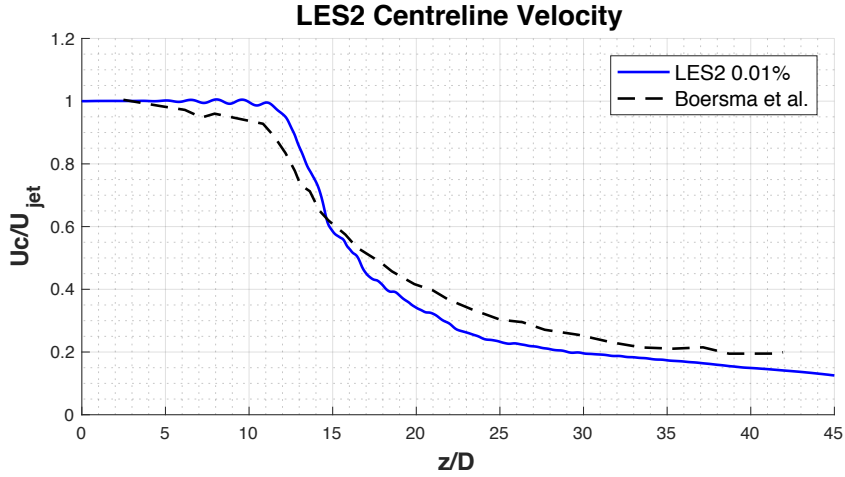


**Figure 20:** Centreline velocity of the LES2 simulation compared with the results of Boersma et al. [2].

The centreline plot of the LES2 (Figure 14) simulation resembles the DNS2 simulation a lot. LES2 is of course better converged due to the prolonged simulation time. Both DNS2 and LES2 place the jet break up point further from orifice than Boersma et al. [2]. This is in disagreement with DNS3 which must be considered at least more accurate than DNS2 due to the superior spatial resolution. Figure 21 shows the axial velocity profiles of the LES2 simulation.

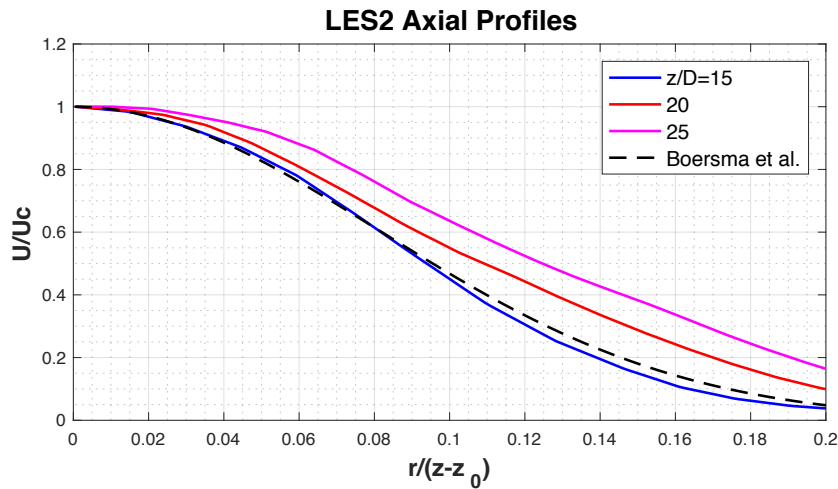


**Figure 21:** Axial velocity profiles at  $z/D=15$ , 20, and 25 plotted with the Gaussian function fit of Boersma et al. [2].

The axial velocity profile at  $z=15D$  fit the expected Gaussian function well. However, it is evident that the discrepancy increases with distance from orifice (Figure 21). This is likely an effect of insufficient spatial resolution in the Far Field which was also mentioned when discussing the DNS3 results. Key parameters of the LES2 simulation are summarized in Table 4. The half-radius spreading rate of  $A=0.13$  shows that the LES2 simulation generally overestimates the width of the jet. This behavior can also

be seen on the axial profile plot. The LES2 results are generally promising though and will most likely improve a lot with Far Field mesh refinement.

**Table 4:** Table summarizing key jet parameters obtained from the DNS3 and the LES2 simulations. The table also includes constants from researchers presented in the general theory section.  $A$  is spreading rate of the half-radius,  $B_u$  is the decay constant, and  $z_0$  is the virtual origin.

<b>Authors</b>	$A$	$B_u$	$z_0$
DNS3 0.01%	0.09	6	0.9
LES2 0.01%	0.13	4.9	5.5
Boersma et al. [2]	-	5.9	4.9
Fellouah et al.[3]	0.097	5.59	2.5

## 4 Conclusion

A turbulent round jet issuing from an wall-mounted orifice was simulated at a low Reynolds number of 2400 by means of DNS and LES. The simulations lay the basic groundwork for a LES study of a jet at a much higher and more computationally demanding Reynolds number of 20,000.

It was first attempted to perform a DNS simulation of the jet under conditions similar to those described by Boersma et al. [2]. The initial simulations using a relatively coarse mesh showed promising results in regard to the evolution of the centreline velocity. However, upon several mesh refinements, it was discovered that no so-called natural transition to turbulence would occur as the spatial resolution was improved. The turbulence created by the initial velocity perturbation was being damped and the flow field approached a laminar state with time. In the persistent attempt to achieve natural transition to turbulence, a velocity profile emulating that of a strong contraction nozzle was introduced. Simulations with the contraction profile showed that this profile was simply accelerating the transition to a laminar-like flow field. Thus the uniform inlet profile provided the best conditions for turbulent behavior though it was not possible to replicate the natural transition to turbulence reported by Boersma et al. [2] in the present study.

Uncorrelated inlet noise was then superimposed on the uniform inlet profile, successfully leading to turbulent behavior. Multiple noise levels were investigated and the breakup of the jet proved to be fairly sensitive to this disturbance. It was found that fluctuations of 0.01% produced results comparable to Boersma et al. [2]. The best simulation of the present study, DNS3, was carried out with a 4 million cell mesh and inlet noise in the order of 0.01%. The DNS3 jet breaks early because of the inlet noise, however, the mean statistics are in excellent agreement with Boersma et al. [2]. The half-radius spreading rate of  $A=0.09$  correspond well to experimental values typically found to be close to  $A=0.1$ . The decay constant of  $B_u = 6$  is very close to the value  $B_u = 5.9$  found by Boersma et al. [2]. The self-similar axial profiles fit almost perfectly as well.

It was then attempted to perform a LES simulation on coarser mesh of 1 million cells as this method would be the feasible way to accurately simulate jets of higher Reynolds numbers. The results of the LES simulation were not equivalent to the results of the DNS3 simulation. Nevertheless, the results were promising, especially when looking at the axial profile at  $z = 15D$  as it is very close to the expected Gaussian function.



## 5 Further Work

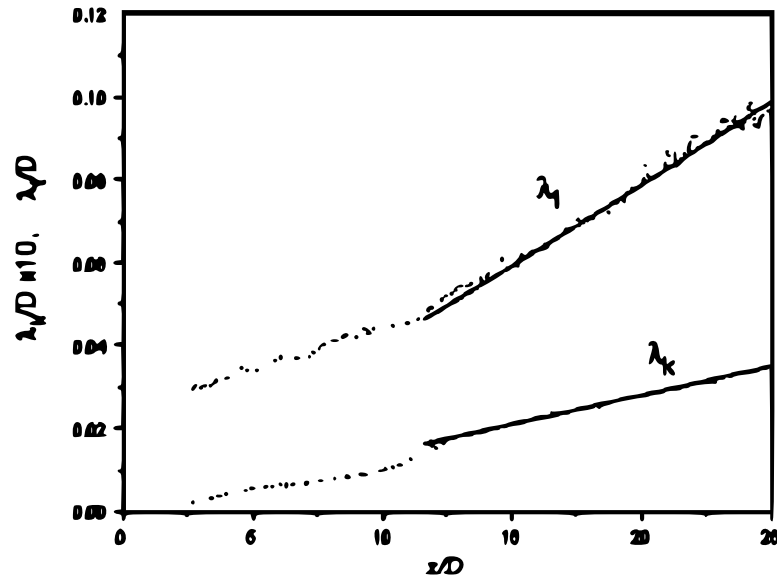
This study lays the groundwork for further work towards accurately simulating the  $Re = 20,000$  jet with LES. The half-radius spreading rate, the centreline velocity decay constant and the self-similar axial profiles of the DNS3 simulation agree well with literature. However, the results of DNS2 and DNS3 are significantly different and thus an additional mesh refinement would be needed to ensure grid independence of the DNS simulations. The LES simulation would then have to be investigated further until not only mean statistics but also turbulence statistics are comparable to that of the DNS as turbulence statistics are the real interest of PhD student Azur Hodzic. If comparable, an LES simulation could be carried out with a refined mesh. The natural transition is not a concern as it will most likely occur more easily at a Reynolds number of 20,000.

## References

- [1] C.G. Ball, H. Fellouah, and A. Pollard. “The flow field in turbulent round free jets”. In: *Progress in Aerospace Sciences* 50 (2012), pp. 1–26. ISSN: 0376-0421. DOI: <https://doi.org/10.1016/j.paerosci.2011.10.002>.
- [2] B. J. Boersma, G. Brethouwer, and F. T. M. Nieuwstadt. “A numerical investigation on the effect of the inflow conditions on the self-similar region of a round jet”. In: *Physics of Fluids* 10.4 (1998), pp. 899–909. DOI: [10.1063/1.869626](https://doi.org/10.1063/1.869626).
- [3] Hachimi Fellouah and Andrew Pollard. “The velocity spectra and turbulence length scale distributions in the near to intermediate regions of a round free turbulent jet”. In: *Physics of Fluids* 21.11 (2009), p. 115101. DOI: [10.1063/1.3258837](https://doi.org/10.1063/1.3258837).
- [4] Hussein J. Hussein, Steven P. Capp, and William K. George. “Velocity measurements in a high-Reynolds-number, momentum-conserving, axisymmetric, turbulent jet”. In: *Journal of Fluid Mechanics* 258 (1994), pp. 31–75. DOI: [10.1017/S002211209400323X](https://doi.org/10.1017/S002211209400323X).
- [5] N. R. Panchapakesan and J. L. Lumley. “Turbulence measurements in axisymmetric jets of air and helium. Part 1. Air jet”. In: *Journal of Fluid Mechanics* 246 (1993), pp. 197–223. DOI: [10.1017/S0022112093000096](https://doi.org/10.1017/S0022112093000096).
- [6] Stephen B. Pope. *Turbulent Flows*. Cambridge University Press, 2000. DOI: [10.1017/CB09780511840531](https://doi.org/10.1017/CB09780511840531).
- [7] I. Wygnanski and H. Fiedler. “Some measurements in the self-preserving jet”. In: *Journal of Fluid Mechanics* 38.3 (1969), pp. 577–612. DOI: [10.1017/S0022112069000358](https://doi.org/10.1017/S0022112069000358).

## Appendix

### A Axial Evolution of the Kolmogorov Length Scale



Axial growth of the Kolmogorov length scale and the Taylor microscale adapted from Fellouah et al. [3]. The lower graph is the Kolmogorov length scale and the upper graph is the Taylor microscale.

## B Derivation of The Kolmogorov Length Scale Growth

Starting with dissipation rate from Panchapakesan and Lumley [5]:

$$\frac{r_{1/2}}{U_c^3} \epsilon = 0.017 \leftrightarrow \epsilon = 0.017 \frac{U_c^3}{r_{1/2}}$$

Inserting the dissipation rate in the general relation between the Kolmogorov length scale and the dissipation rate:

$$\eta_k = \left( \frac{\nu^3}{\epsilon} \right)^{1/4} = \left( \frac{\nu^3 r_{1/2}}{0.017 U_c^3} \right)^{1/4}$$

$U_c$  is described by the decay function:

$$U_c = \frac{B_u}{z/D - z_0/D} U_{jet}$$

Thus, the Kolmogorov length scale is given by:

$$\eta_k = \left( \frac{\nu^3 r_{1/2} [z/D - z_0/D]^3}{0.017 B_u^3 U_{jet}^3} \right)^{1/4}$$

Now,  $r_{1/2}$  is approximately given by  $r_{1/2} = 0.1z$  as discussed in the General Theory section. Furthermore, the contribution from  $z_0$  is neglectable in the Far Field so this term is removed. This yields:

$$\eta_k = \left( \frac{\nu^3 z^4}{0.17 B_u^3 U_{jet}^3 D^3} \right)^{1/4}$$

Notice that  $1/Re^3 = \nu^3/(U_{jet}^3 D^3)$ . Hence:

$$\eta_k = \left( \frac{1}{0.17 B_u^3 Re^3} \right)^{1/4} z, \quad z \gg z_0$$

Which simplifies to:

$$\eta_k = (0.17 B_u^3 Re^3)^{-1/4} z, \quad z \gg z_0$$

## C Contraction Profile Momentum Flux

$U_{\text{ref}}$  is adjusted such that the momentum flux of the contraction velocity profile is equivalent to that of the uniform profile. The momentum flux through a control surface is given by:

$$\int_{CS} \vec{U} \rho \vec{U} \cdot \vec{n} \, dA$$

For the uniform profile, this yields:

$$\int_0^R 2r\pi\rho U_{\text{jet}}^2 \, dr = 2\pi\rho U_{\text{jet}}^2 \int_0^R r \, dr$$

For the contraction profile, this yields:

$$\int_0^R 2r\pi\rho U_{\text{ref}}^2 \left[1 - \left(\frac{r}{R}\right)^n\right]^2 \, dr = 2\pi\rho U_{\text{ref}}^2 \int_0^R r \left[1 - \left(\frac{r}{R}\right)^n\right]^2 \, dr$$

The momentum fluxes have to be equal:

$$2\pi\rho U_{\text{jet}}^2 \int_0^R r \, dr = 2\pi\rho U_{\text{ref}}^2 \int_0^R r \left[1 - \left(\frac{r}{R}\right)^n\right]^2 \, dr$$

$U_{\text{ref}}$  is now isolated and the equation is simplified to:

$$U_{\text{ref}} = U_{\text{jet}} \sqrt{\frac{\int_0^R r \, dr}{\int_0^R r \left[1 - \left(\frac{r}{R}\right)^n\right]^2 \, dr}}$$

**DTU Mechanical Engineering**  
**Section of Fluid Mechanics, Coastal and Maritime Engineering**  
Technical University of Denmark

Nils Koppels Allé, Bld. 403  
DK-2800 Kgs. Lyngby  
Denmark  
Phone (+45) 4525 1360  
Fax (+45) 4588 4325

[www.mek.dtu.dk](http://www.mek.dtu.dk)